3D Wave-Equation Dispersion Inversion of Surface Waves

Zhaolun Liu, Jing Li, Sherif M. Hanafy and Gerard Schuster, King Abdullah University of Science and Technology

SUMMARY

The 2D wave-equation dispersion inversion (WD) methodology is extended to the inversion of three-dimensional data for a 3D shear-wave velocity model. The objective function of 3D WD is the sum of the squared wavenumber differences along each azimuth angle between the predicted and observed 3D dispersion curves. The 3D dispersion curves are obtained by wavenumber-frequency analysis of the fundamental Rayleigh waves in each 3D shot gather. The S-wave velocity update is computed by a weighted zero-lag crosscorrelation between the source wavefield and the back-projected receiver-side wavefield for each azimuth angle. The synthetic and field data examples demonstrate that the 3D WD method can accurately estimate the 3D S-wave velocity model in laterally heterogeneous media.

INTRODUCTION

Surface-wave methods are powerful tools for characterizing the near-surface S-velocity distribution. This is because the recorded data are usually dominated by surface waves for a wide range of source-receiver offsets within the time window of surface-wave arrivals. A practical application is that surface waves can be inverted to detect shallow drilling hazards down to the depth on the order of the dominant shear wavelength (Dahlen and Tromp, 1998).

The conventional dispersion-inversion method calculates the S-wave velocity model directly from the surface dispersion curves (Haskell, 1953; Xia et al., 1999, 2002; Park et al., 1999) by assuming a 1D velocity model beneath the recording data. Unfortunately, this assumption is violated when there are strong lateral gradients in the S-velocity model, such as faults, vugs or gas channels.

As an alternative, full-waveform inversion (FWI) (Groos et al., 2014; Pérez Solano et al., 2014; Dou and Ajo-Franklin, 2014; Groos et al., 2017) estimates the S-velocity model that accurately predicts the surface waves recorded in a heterogeneous S-velocity model. But in practice, FWI easily gets stuck in local minima due to the strongly dispersive nature of surface waves and an inadequate initial velocity model. To mitigate this problem, Pérez Solano et al. (2014) changed the misfit function of FWI into the l^2 misfit of the Rayleigh-wave magnitude spectra, and their synthetic data results showed this to be an effective method for reconstructing the S-wave velocity model at the near surface. Until now there are few studies to assess the limitations of this method so its effectiveness on a wider variety of data sets is still to be determined.

To combine the inversion of both surface waves with body waves, Yuan et al. (2015) developed a wavelet multi-scale adjoint method for the joint inversion of both surface and body waves. The efficacy of this method is validated with synthetic data. However, further studies are needed to assess its robustness in convergence. To enhance robustness, a layer stripping strategy for FWI of surface waves was presented by Masoni et al. (2016) who first invert the high-frequency and near-offset data for the shallow S-velocity model, and gradually incorporates lower-frequency data with longer offsets to estimate the deeper parts of the model. All these methods, however, are still under development and require more tests to fully understand their relative benefits and limitations.

To avoid the assumption of a layered medium and also mitigate FWI's sensitivity to local minima, Li and Schuster (2016) and Li et al. (2017c) proposed a new surface-wave dispersion inversion method, which is denoted as wave equation dispersion inversion (WD). Here, they used solutions of the 2D elastic wave equation to form the misfit gradient associated with Rayleigh waves. In this way they avoid the need for a layered medium assumption. Numerical tests on the synthetic data and the field data for 2D models show that WD can accurately reconstruct the S-wave velocity distributions in laterally heterogeneous media. The WD method also enjoys robust convergence because the skeletonized data, namely the dispersion curves, have simpler complexity than traces with many dispersive arrivals. The penalty, however, is that the inverted S-velocity model has lower resolution than a model that accurately fits the waveforms. Thus, the WD tomogram can serve as a good starting model for surface-wave FWI.

In this paper, we extend the 2D WD method to invert for the 3D S-wave velocity model that accounts for strong velocity variations in all three dimensions. After the introduction, we describe the theory of 3D WD. Numerical tests on synthetic and field data are presented in the second section to validate the theory. The 3D Foothills model in the synthetic test is related to that from the SEAM consortium. The field data were recorded by a seismic experiment we conducted near the KAUST campus in Saudi Arabia. The summary is given in the last section.

THEORY

Let $d(\boldsymbol{g},t)$ denote a shot gather of vertical particle-velocity traces recorded by the receiver on the surface at $\boldsymbol{g} = (x_g, y_g, 0)$ and excited by a vertical-component point source at $\boldsymbol{s} = (x_s, y_s, 0)$, where $z = 0$ is the depth of the horizontal recording plane. We will assume that the effects of attenuation on the dispersion curves are insignificant. But, if important, such effects can be accounted for by using solutions to viscoelastic wave equation (Li et al., 2017a,b). Assume $d(\boldsymbol{g},t)$ only contains the fundamental mode of Rayleigh waves. We apply the 3D Fourier transform to $d(\boldsymbol{g},t)$ to get $\tilde{D}(\boldsymbol{k},\omega)$ in the $\boldsymbol{k} - \omega$ domain,

$$\tilde{D}(\boldsymbol{k},\omega) = \int\int d(\boldsymbol{g},t)e^{-i(\boldsymbol{k}\cdot\boldsymbol{g}+\omega t)}d\boldsymbol{g}dt = \int D(\boldsymbol{g},\omega)e^{-i\boldsymbol{k}\cdot\boldsymbol{g}}d\boldsymbol{g}.$$

$$(1)$$

where $d\boldsymbol{g} = dx_g dy_g$ and $D(\boldsymbol{g},\omega)$ represents the data in the space-frequency $(\boldsymbol{x} - \omega)$ domain. Here, the $z = 0$ notation is silent. The wavenumber vector $\boldsymbol{k} = (k_x, k_y)$ can be represented in polar coordinate as (k, θ), where $\theta = \arctan \frac{k_y}{k_x}$ is the azimuth angle and $k = \sqrt{k_x^2 + k_y^2}$ is the radius. Following this notation, the Fourier transformed data $\tilde{D}(\boldsymbol{k}, \omega)$ are denoted as $\tilde{D}(k, \theta, \omega)$. We skeletonize the spectrum $\tilde{D}(k, \theta, \omega)$ as the surface-wave dispersion curves, which are the wavenumbers $\kappa(\theta, \omega)$ obtained by picking the (k, θ, ω) coordinates of the maximum magnitude spectrum $\tilde{D}(k, \theta, \omega)$ along the azimuth angle θ. In this paper, we assume that the dispersion curves are those for Rayleigh waves recorded by vertical-component geophones, but this approach is also valid for Love waves.

Misfit Function

The 3D WD method inverts for the S-wave velocity model that minimizes the objective function of the dispersion curves:

$$\varepsilon = \frac{1}{2} \sum_\omega \sum_\theta \overbrace{[\kappa(\theta, \omega)_{pre} - \kappa(\theta, \omega)_{obs}}^{residual = \Delta\kappa(\theta,\omega)}]^2 + \text{penalty term}, \quad (2)$$

where the penalty term can be any model-based function that penalizes solutions far from an apriori model. Here, $\kappa(\theta, \omega)_{pre}$ represents the predicted dispersion curve picked from the simulated spectrum along the azimuth angle θ and $\kappa(\theta, \omega)_{obs}$ describes the observed dispersion curve obtained from the recorded spectrum along the azimuth θ. For pedagogical clarity, we will ignore the penalty term.

Gradient

The gradient $\gamma(\boldsymbol{x})$ of ε with respect to the S-wave velocity $v_s(\boldsymbol{x})$ is given by

$$\gamma(\boldsymbol{x}) = \frac{\partial \varepsilon}{\partial v_s(\boldsymbol{x})} = \sum_\omega \sum_\theta \Delta\kappa(\theta, \omega) \frac{\partial \kappa(\theta, \omega)_{pre}}{\partial v_s(\boldsymbol{x})},$$

$$= -\sum_\omega \sum_\theta \Delta\kappa(\theta, \omega) \frac{\Re\left\{ \int d\boldsymbol{g} \frac{\partial D(\boldsymbol{g},\omega)}{\partial v_s(\boldsymbol{x})} \hat{D}(\boldsymbol{g}, \theta, \omega)^*_{obs} \right\}}{A}, \quad (3)$$

where A is the normalization term

$$A = \Re\left\{ \int \ddot{\tilde{D}}(k + \Delta\kappa, \theta, \omega)^*_{obs} \tilde{D}(k, \theta, \omega) dk \right\}, \quad (4)$$

in which $\dot{\tilde{D}}(k, \theta, \omega)_{obs} = \frac{\partial \tilde{D}(k + \Delta\kappa, \theta, \omega)_{obs}}{\partial \Delta\kappa}$. $\hat{D}(\boldsymbol{g}, \theta, \omega)^*_{obs}$ is the weighted conjugated data function:

$$\hat{D}(\boldsymbol{g}, \theta, \omega)^*_{obs} = 2\pi i \boldsymbol{g} \cdot \boldsymbol{n} e^{i\boldsymbol{g} \cdot \boldsymbol{n} \Delta\kappa} \int_C D(\boldsymbol{g}'(\boldsymbol{g}, \theta), \omega)^*_{obs} d\boldsymbol{g}', \quad (5)$$

in which $\boldsymbol{n} = (\cos\theta, \sin\theta)$ and C is the line $(\boldsymbol{g}' - \boldsymbol{g}) \cdot \boldsymbol{n} = 0$.

$\frac{\partial D(\boldsymbol{g},\omega)}{\partial v_s(\boldsymbol{x})}$ can be obtained according to the Born approximation for elastic waves,

$$\frac{\partial D(\boldsymbol{g}, \omega)}{\partial v_s(\boldsymbol{x})} = 4 v_{s0}(\boldsymbol{x}) \rho_0(\boldsymbol{x}) \Big[G_{3k,k}(\boldsymbol{g}|\boldsymbol{x}) D_{j,j}(\boldsymbol{x}, \omega)$$
$$- \frac{1}{2} G_{3n,k}(\boldsymbol{g}|\boldsymbol{x}) \big[D_{k,n}(\boldsymbol{x}, \omega) + D_{n,k}(\boldsymbol{x}, \omega) \big] \Big], \quad (6)$$

where $v_{s0}(\boldsymbol{x})$ and $\rho_0(\boldsymbol{x})$ are the reference S-velocity and density models, respectively, at location $\boldsymbol{x}$. $D_i(\boldsymbol{x}, \omega)$ denotes the ith component of the particle velocity recorded at $\boldsymbol{x}$ due to a vertical-component force. Einstein notation is assumed in equation 6 where $D_{i,j} = \frac{\partial D_i}{\partial x_j}$ for $i, j \in \{1, 2, 3\}$. The 3D harmonic Green's tensor $G_{3j}(\boldsymbol{g}|\boldsymbol{x})$ is the particle velocity at location $\boldsymbol{g}$ along the jth direction due to a vertical-component force at $\boldsymbol{x}$ in the reference medium.

Gradient Update

The optimal S-wave velocity model $v_s(\boldsymbol{x})$ can be obtained from the steepest-descent formula (Nocedal and Wright, 2006)

$$v_s(\boldsymbol{x})^{(k+1)} = v_s(\boldsymbol{x})^{(k)} - \alpha \frac{\partial \varepsilon}{\partial v_s(\boldsymbol{x})}, \quad (7)$$

where α is the step length and the superscript (k) denotes the kth iteration. In practice, a preconditioned conjugate gradient method is used, where source illumination is used as the preconditioning factor (Luo and Schuster, 1991).

NUMERICAL EXAMPLES

Modified Foothills Model

The modified 3D Foothills S-wave velocity model is shown in Figure 1a. The P-wave velocity is defined as $v_p = \sqrt{3} v_s$. An areal acquisition array is distributed on the surface and 400 vertical-component shot gathers are computed with a 60 m spacing in both the x and y directions with a 50×50 geophone array. The geophone spacing is 24 m. The peak frequency of the source is 20 Hz and the observed data are recorded for 0.99 seconds with a 0.3 ms sampling rate. The initial S-wave velocity model for 3D WD is shown in Figure 1b. For each
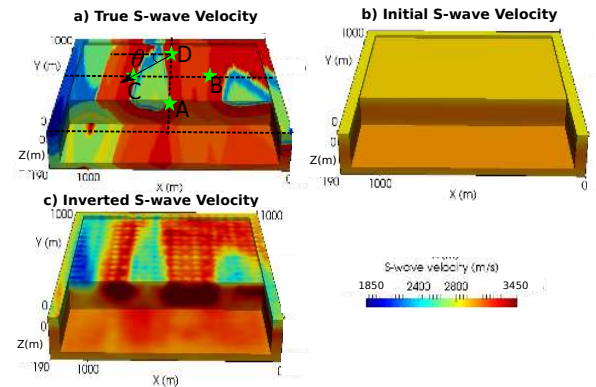

Figure 1: S-velocity model modified from the Foothills model, where the stars indicate the locations of sources A, B, C and D on the surface, and θ is the azimuth angle with respect to the coordinate system centered at source D.

shot gather, only the receivers within the distance $r_1 = 600$ m from the source are used to retrieve the dispersion curves. The fundamental dispersion curves for each shot gather are picked along the dominant azimuths from $0°$ to $360°$ with an interval of $3°$ in the $k_x - k_y - f$ domain. For example, Figure 2 shows the observed dispersion curves calculated from the CSGs for

the sources located at points A, B, C and D indicated in Figure 1a, where the black dashed lines represent the contours of the observed dispersion curves. The cyan dash-dot lines in Figure 2 represent the contours of the initial dispersion curves. Figure 1c displays the inverted S-wave velocity model after 15
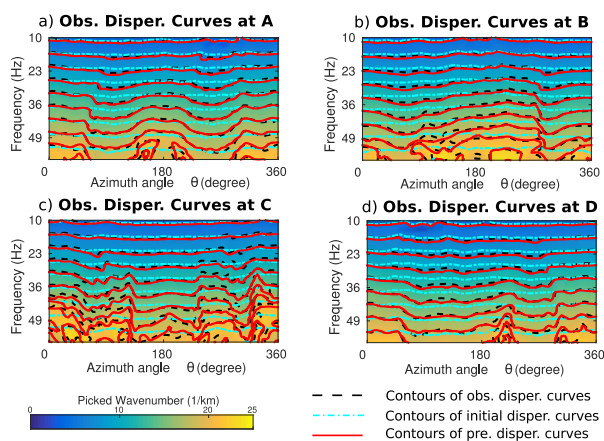

Figure 2: The observed dispersion curves for (a) source A, (b) source B, (c) source C and (d) source D indicated in Figure 1a, where the black dashed lines, the cyan dash-dot lines and the red lines represent the contours of the observed, initial and inverted dispersion curves, respectively.

iterations, which agrees well with the actual model down to a depth of about 1/3 the dominant wavelength. The contours of the predicted dispersion curves for the sources at A, B, C and D are represented by the red lines in Figure 2, which agree well with the contours of the observed dispersion curves.

Qademah Fault Seismic Data
A 3D land survey was carried out along the Red Sea coast over the Qademah fault system, about 30 km north of the KAUST campus (Hanafy et al., 2015). The survey consisted of 288 receivers arranged along 12 parallel lines, and each line has 24 receivers. The inline receiver interval is 5 m and the crossline interval is 10 m. The receiver geometry is shown in Figure 3, where one shot is fired at each receiver location for a total of 288 shot gathers. The observed data are recorded for 0.7 seconds with a 4 ms sampling rate. 2D WD is first applied to the inline data to invert for twelve 2D S-velocity models. We interpolate these 2D velocity models to obtain an initial velocity model for 3D WD, which is shown in Figure 4a.

For each shot gather, only the receivers within the distance $r_1 = 50$ m from the source are used to retrieve the dispersion curves. The frequency range used in WD is from 20 Hz to 60 Hz. The fundamental dispersion values calculated from CSGs for the sources located at A, B, C and D, which are indicated in Figure 3, are displayed in Figure 5, where the black dashed lines represent the contours of the observed dispersion curves. For some frequency ranges, it is difficult to pick the dispersion curves because of the low signal-to-noise ratio of the data so that some dispersion curves are missing in Figure 5. The contours of the initial dispersion curves are represented by the cyan lines in Figure 5.

The S-wave velocity tomogram is shown in Figure 4b, where the red line labeled with "F1" indicates the location of the Qademah fault and the red line labeled with "F2" may be interpreted as a small antithetic fault. The low-velocity anomaly between the two faults is interpreted as a colluvial wedge labeled with "CW". The red dash-dot lines in Figure 5 show the predicted $\kappa(\omega)$ curves calculated from the CSGs with sources located at A, B, C and D indicated in Figure 3. It is evident that the WD tomogram has decreased the differences between the initial and observed dispersion values.

Figures 6 and 7 show the comparison of the observed (blue) and synthetic (red) traces No. 1-288 of CSG No. 1, where the synthetic data are calculated from the (a) initial and (b) inverted S-velocity models. "FM" and "HM" represent fundamental- and higher-mode surface waves, respectively. We can see that the predicted fundamental-mode surface waves closely match the observed ones regardless of the waveform. The predicted higher-mode surface waves correlate well with those of the observed data even though we only invert the dispersion curves of fundamental modes.

Slices of the S-wave velocity tomogram are shown in Figure 8a and the dashed lines indicate the locations of the conjectured Qademah fault. The blue low-velocity zone (LVZ) in Figure 8a next to the conjectured fault is consistent with the downthrown-side of an interpreted normal fault. The LVZ is also consistent with the reflectivities of the migration image (Liu et al., 2016, 2017) indicated by the blue zone next to the dashed fault in Figure 8b. This LVZ next to the fault is accompanied by a delay in the surface-wave arrivals shown in the common offset gathers (COG) in Figure 8c.

CONCLUSIONS

We extend the 2D WD methodology to 3D, where the objective function is the sum of the squared differences between the wavenumbers along the predicted and observed dispersion curves for each azimuth angle. The S-wave velocity update is computed by migrating the weighted data for each azimuth angle. The synthetic and field data examples demonstrate that the WD method can reconstruct the 3D S-wave velocity tomograms of a laterally heterogeneous media so that the predicted surface waves closely math the observed ones for the fundamental modes.
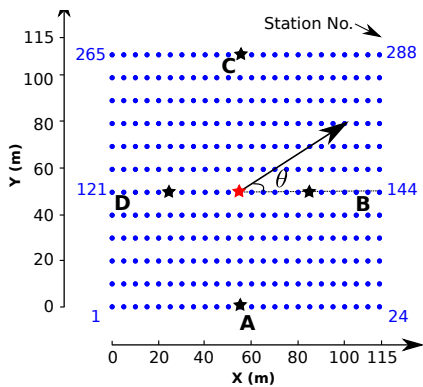
Figure 3: Receiver geometry for the Qademah-fault data. Shots were located at each geophone. The blue dots represent the locations of receivers, and the red star represents the location of source #132. The black stars indicate the locations of sources A, B, C and D on the surface. θ is the azimuth angle for source #132.
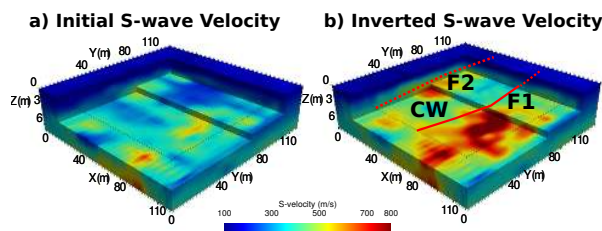

Figure 4: (a) initial and (b) inverted S-wave velocity models. The red solid line labeled by "F1" indicates the location of the conjectured Qademah fault. The dashed red line labeled by "F2" is conjectured to be a small antithetic fault. The low-velocity anomaly between faults "F1" and "F2" is the conjectured colluvial wedge labeled by "CW".
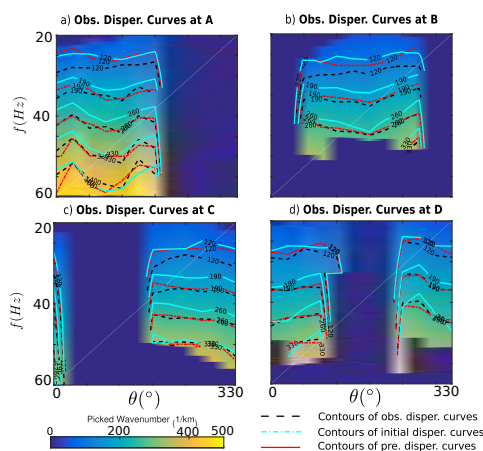

Figure 5: Observed dispersion curves for (a) source A, (b) source B, (c) source C and (d) source D indicated in Figure 3. The black dashed lines, the cyan lines and the red dash-dot lines represent the contours of the observed, initial and inverted dispersion curves, respectively.
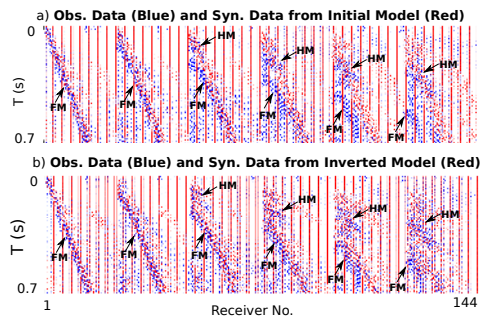

Figure 6: Comparison of the observed (blue) and synthetic (red) traces No. 1-144 of CSG No. 1, where the synthetic data are calculated from a) initial and b) inverted S-velocity model. "FM" and "HM" represent fundamental- and higher-mode surface waves, respectively.
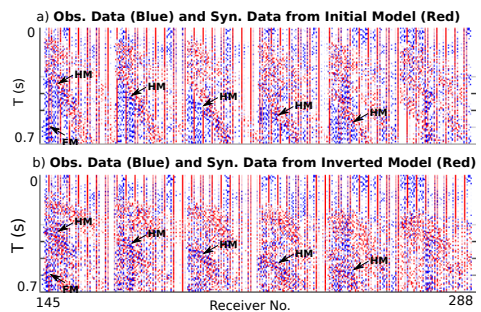

Figure 7: Comparison of the observed (blue) and synthetic (red) traces No. 145-288 of CSG No. 1, where the synthetic data are calculated from a) initial and b) inverted S-velocity model. "FM" and "HM" represent fundamental- and higher-mode surface waves, respectively.
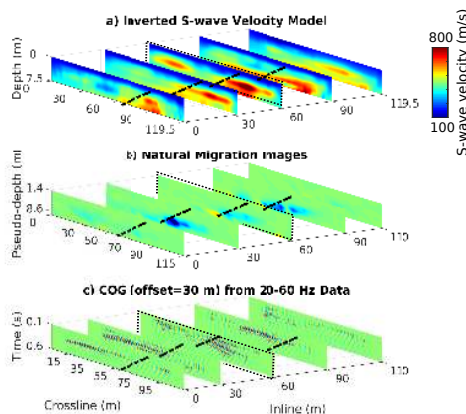

Figure 8: Slices of a) the inverted S-wave velocity model, b) natural migration images (Liu et al., 2017) and c) common offset gathers (offset is 30 m). The dashed lines indicate the location of the interpreted Qademah fault.

REFERENCES

Dahlen, F., and J. Tromp, 1998, Theoretical Global Seismology: Princeton University Press.

Dou, S., and J. B. Ajo-Franklin, 2014, Full-wavefield inversion of surface waves for mapping embedded low-velocity zones in permafrost: Geophysics, **79**, no. 6, EN107–EN124, https://doi.org/10.1190/geo2013-0427.1.

Groos, L., M. Schäfer, T. Forbriger, and T. Bohlen, 2014, The role of attenuation in 2D full-waveform inversion of shallow-seismic body and Rayleigh waves: Geophysics, **79**, no. 6, R247–R261, https://doi.org/10.1190/geo2013-0462.1.

Groos, L., M. Schäfer, T. Forbriger, and T. Bohlen, 2017, Application of a complete workflow for 2D elastic full-waveform inversion to recorded shallow-seismic Rayleigh waves: Geophysics, **82**, no. 2, R109–R117, https://doi.org/10.1190/geo2016-0284.1.

Hanafy, S. M., 2015, Mapping the Qademah fault with traveltime, surface-wave, and resistivity tomograms: 85th Annual International Meeting, SEG, Expanded Abstracts, 3347–3351, https://doi.org/10.1190/segam2015-5886064.1.

Haskell, N. A., 1953, The dispersion of surface waves on multilayered media: Bulletin of the Seismological Society of America, **43**, 17–34.

Li, J., G. Dutta, and G. Schuster, 2017a, Wave-equation Qs inversion of skeletonized surface waves: Geophysical Journal International, **209**, 979–991, https://doi.org/10.1093/gji/ggx051.

Li, J., G. Dutta, and G. Schuster, 2017b, Skeletonized wave-equation Qs tomography using surface waves: 87th Annual International Meeting, SEG, Expanded Abstracts, 2726–2731, https://doi.org/10.1190/segam2017-17784736.1.

Li, J., Z. Feng, and G. Schuster, 2017c, Wave-equation dispersion inversion: Geophysical Journal International, **208**, 1567–1578, https://doi.org/10.1093/gji/ggw465.

Li, J., and G. Schuster, 2016, Skeletonized wave equation of surface wave dispersion inversion: 86th Annual International Meeting, SEG, Expanded Abstracts, 3630–3635, https://doi.org/10.1190/segam2016-13770057.1.

Liu, Z., A. Altheyab, S. Hanafy, and G. Schuster, 2016, Imaging near-surface heterogeneities by natural migration of surface waves: 86th Annual International Meeting, SEG, Expanded Abstracts, 4946–4950, https://doi.org/10.1190/segam2016-13845123.1.

Liu, Z., A. AlTheyab, S. M. Hanafy, and G. Schuster, 2017, Imaging near-surface heterogeneities by natural migration of backscattered surface waves: Field data test: Geophysics, **82**, no. 3, S197–S205, https://doi.org/10.1190/geo2016-0253.1.

Luo, Y., and G. T. Schuster, 1991, Wave-equation traveltime inversion: Geophysics, **56**, 645–653, https://doi.org/10.1190/1.1443081.

Masoni, I., J.-L. Boelle, R. Brossier, and J. Virieux, 2016, Layer stripping FWI for surface waves: 86th Annual International Meeting, SEG, Expanded Abstracts, 1369–1373, https://doi.org/10.1190/segam2016-13859781.1.

Nocedal, J., and S. Wright, 2006, Numerical optimization: Springer Science & Business Media.

Park, C. B., R. D. Miller, and J. Xia, 1999, Multichannel analysis of surface waves: Geophysics, **64**, 800–808, https://doi.org/10.1190/1.1444590.

Pérez Solano, C. A., D. Donno, and H. Chauris, 2014, Alternative waveform inversion for surface wave analysis in 2-D media: Geophysical Journal International, **198**, 1359–1372, https://doi.org/10.1093/gji/ggu211.

Xia, J., R. Miller, C. Park, and G. Tian, 2002, Determining Q of near-surface materials from Rayleigh waves: Journal of Applied Geophysics, **51**, 121–129, https://doi.org/10.1016/s0926-9851(02)00228-8.

Xia, J., R. D. Miller, and C. B. Park, 1999, Estimation of near-surface shear-wave velocity by inversion of Rayleigh waves: Geophysics, **64**, 691–700, https://doi.org/10.1190/1.1444578.

Yuan, Y. O., F. J. Simons, and E. Bozdăg, 2015, Multiscale adjoint waveform tomography for surface and body waves: Geophysics, **80**, no. 5, R281–R302, https://doi.org/10.1190/geo2014-0461.1.